THE EUROPEAN
PHYSICAL JOURNAL A

High-precision mass measurement of doubly magic ²⁰⁸Pb

Kathrin Kromer[1,a] , **Chunhai Lyu**[1] , **Menno Door**[1] , **Pavel Filianin**[1] , **Zoltán Harman**[1], **Jost Herkenhoff**[1] ,
Wenjia Huang[2] , **Christoph H. Keitel**[1] , **Daniel Lange**[1,3] , **Yuri N. Novikov**[4,5] , **Christoph Schweiger**[1] ,
Sergey Eliseev[1] , **Klaus Blaum**[1]

[1] Max-Planck-Institut für Kernphysik, 69117 Heidelberg, Germany
[2] Advanced Energy Science and Technology Guangdong Laboratory, Huizhou 516007, China
[3] Ruprecht-Karls-Universität Heidelberg, 69117 Heidelberg, Germany
[4] Department of Physics, St Petersburg State University, Saint Petersburg 198504, Russia
[5] NRC "Kurchatov Institute" Petersburg Nuclear Physics Institute, Gatchina 188300, Russia

Abstract The absolute atomic mass of ²⁰⁸Pb has been
determined with a fractional uncertainty of 7×10^{-11} by
measuring the cyclotron-frequency ratio R of ²⁰⁸Pb⁴¹⁺ to
¹³²Xe²⁶⁺ with the high-precision Penning-trap mass spec-
trometer PENTATRAP and computing the binding energies
E_{Pb} and E_{Xe} of the missing 41 and 26 atomic elec-
trons, respectively, with the *ab initio* fully relativistic multi-
configuration Dirac–Hartree–Fock (MCDHF) method. R has
been measured with a relative precision of 9×10^{-12}. E_{Pb}
and E_{Xe} have been computed with an uncertainty of 9.1 eV
and 2.1 eV, respectively, yielding 207.976 650 571(14) u
(u = $9.314\,941\,024\,2(28) \times 10^{8}$ eV/c²) for the ²⁰⁸Pb neutral
atomic mass. This result agrees within 1.2σ with that from the
Atomic-Mass Evaluation (AME) 2020, while improving the
precision by almost two orders of magnitude. The new mass
value directly improves the mass precision of 14 nuclides
in the region of $Z = 81$–84 and is the most precise mass
value with $A > 200$. Thus, the measurement establishes a
new region of reference mass values which can be used e.g.
for precision mass determination of transuranium nuclides,
including the superheavies.

1 Introduction

Heavy and superheavy nuclides beyond the doubly magic
nucleus of ²⁰⁸Pb can only exist due to nuclear shell effects
holding them together by counteracting the rapidly increas-
ing Coulomb repulsion with growing proton number Z
[1]. Insight into these quantum-mechanical nuclear structure
effects can be derived from the masses of such nuclides. In

addition to some direct heavy mass measurements [2–5], a
network of nuclear transitions and relative mass measure-
ments, i.e. the *Atomic-Mass Evaluation* (AME), provides
mass values for most heavy and superheavy nuclides by
tracing them back to a few well-known masses of uranium
isotopes [6]. However, no nuclide beyond $Z = 70$ can be
found whose mass is known to a relative precision of better
than 2×10^{-9} to act as a precise reference point for these
heavy elements. This directly limits the achievable precision
in the heavier mass regions and can possibly lead to tensions
or shifts of the relative measured masses due to their refer-
encing to only one reference point. The limitations by mass
dependent shifts can be reduced significantly once there is
a reference mass with similar mass known to high precision
[7]. The need for new anchor points for the AME arose during
recent mass measurements with TRIGA-TRAP [5,8] at the
research reactor TRIGA in Mainz, specifically, an improved
absolute mass of ²⁰⁸Pb [9]. Measuring this mass will also
directly improve the masses of several Pb isotopes and other
nuclides in this mass region [6].

In addition to the impact as a mass reference for other
mass measurements, the mass of ²⁰⁸Pb will soon be needed
when the magnetic moment, or the g-factor, of the bound
electron of hydrogen-like ²⁰⁸Pb is planned to be determined
by the Penning-trap experiments Alphatrap at the MPIK in
Heidelberg [10] and Artemis at GSI Darmstadt [11]. This
measurement could be the most stringent test of bound-state
quantum electrodynamics in strong fields. The error of the
mass of the nucleus, however, enters the error budget and
therefore needs to be known to high precision [12]. With the
results of this paper, the error of the mass of ²⁰⁸Pb will be
negligible in future g-factor determinations.

ᵃ e-mail: kathrin.kromer@mpi-hd.mpg.de (corresponding author)

Based on the accurate absolute mass of ^{132}Xe [13,14], in this paper, we present a determination of the absolute atomic mass of ^{208}Pb with a fractional uncertainty of 7×10^{-11}. This is the result of measuring the cyclotron-frequency ratio of ^{208}Pb^{41+} and ^{132}Xe^{26+} with the high-precision Penning-trap mass spectrometer PENTATRAP [15,16] in combination with a computation of the binding energies of the missing 41 and 26 atomic electrons, respectively, using the *ab initio* fully relativistic multi-configuration Dirac–Hartree–Fock (MCDHF) method. The masses of ^{132}Xe^{26+} and ^{208}Pb^{41+} can be related to their neutral counterparts via

$$m\left(^{132}\text{Xe}^{26+}\right) = m\left(^{132}\text{Xe}\right) - 26m_e + E_{\text{Xe}}, \tag{1}$$

$$m\left(^{208}\text{Pb}^{41+}\right) = m\left(^{208}\text{Pb}\right) - 41m_e + E_{\text{Pb}}, \tag{2}$$

with $m_e = 5.485\,799\,090\,65(16) \times 10^{-4}$ u being the electron rest mass [17] and $m\left(^{132}\text{Xe}\right) = 131.904\,155\,086(10)$ u being the mass of a neutral ^{132}Xe atom [13,14], each has a relative accuracy of 2.9×10^{-11} and 7.6×10^{-11}, respectively. E_{Xe} and E_{Pb} are the binding-energy differences that represent the energies required to ionize the outermost 26 and 41 electrons, respectively, from neutral Xe and Pb atoms. With the mass ratio

$$R = \frac{m\left(^{208}\text{Pb}^{41+}\right)}{m\left(^{132}\text{Xe}^{26+}\right)} \tag{3}$$

being experimentally measured, one can improve the accuracy of the absolute mass of ^{208}Pb via

$$
\begin{aligned}
&m\left(^{208}\text{Pb}\right) \\
&= R\left[m\left(^{132}\text{Xe}\right) + 26m_e - E_{\text{Xe}}\right] \\
&\quad + 41m_e - E_{\text{Pb}},
\end{aligned}
\tag{4}
$$

based on the theoretically calculated E_{Xe} and E_{Pb}. By improving the mass of ^{208}Pb the masses of other Pb isotopes and nearby elements can be improved accordingly since they are linked via decays of which the energy has been measured.

2 Experimental and theoretical methods

If one introduces a charged particle into a magnetic field B, it will describe a free space cyclotron motion with the frequency $\omega_c = \frac{q}{m}B$, with q/m being the charge-to-mass ratio. The working principle of a Penning trap is based on a strong homogeneous magnetic field in combination with an electrostatic quadrupole potential. While the electrostatic potential prevents the ion from escaping in axial direction, forcing it onto an oscillatory axial motion with frequency ω_z, the magnetic field forces the ion in radial direction onto a circular orbit with a modified cyclotron frequency ω_+. The

cross product of the two fields in the Lorentz equation leads to an additional slow drift around the trap center called magnetron motion with frequency ω_-. When comparing these three Penning-trap eigenfrequencies to the movement of a free charged particle in a purely magnetic field, it holds [18]:

$$\omega_c = \sqrt{\omega_+^2 + \omega_z^2 + \omega_-^2}. \tag{5}$$

From this equation we can see that the determination of eigenfrequencies of an ion in a Penning trap can be used to determine its mass, if the magnetic field inside the trap is known. However, a determination of a magnetic field of $B \approx 7$ T inside a volume of just a few 10 μm^3 to sufficient precision is not possible. Therefore, a relative measurement is chosen at PENTATRAP, using a reference ion and a sequential measurement scheme to determine mass ratios [15]. Highly charged ions are used due to the advantage that with higher q/m the modified cyclotron frequency increases and can therefore be measured to a higher relative precision. For each mass determination a reference nuclide and charge states have to be chosen that form a q/m doublet with the nuclide of interest in order to largely suppress systematic effects in the cyclotron-frequency ratio determination [15,16]. The advantage being, that with q/m doublets the same trapping voltage can be used to match the axial frequency to the detection tank circuit's resonance frequency. Using the same trapping voltage reduces systematic shifts due to trap anharmonicities. In addition, the absolute mass of the reference nuclide has to be known better than the aimed uncertainty of the mass of the nuclide of interest. More technical restrictions are posed by the production of the reference ion, limited by binding energies and the availability of probe material. For these reasons, the near q/m doublet ^{208}Pb^{41+} ($q/m = 0.197\,138\,e$/u) and ^{132}Xe^{26+} ($q/m = 0.197\,113\,e$/u) [13,14] was chosen. The ^{132}Xe^{26+} ion was created from a gaseous natural source inside a commercial *Dresden electron beam ion trap* (DREEBIT) [19,20]. The DREEBIT is connected to a beamline with a large bender magnet for q/m selection, see Fig. 1a upper beamline. The ^{208}Pb^{41+} ion was produced in a Heidelberg Compact electron beam ion trap (compact EBIT) [21] equipped with an in-trap laser-desorption target of monoisotopic ^{208}Pb [22]. After ion breeding, the q/m selection was achieved using the time-of-flight separation technique with fast high-voltage switches recently developed at the MPIK [23], supplying the voltages to a Bradbury-Nielsen gate [24], see Fig. 1a lower beamline. Once the ions were selected and decelerated by two pulsed drift tubes, they were consecutively trapped in the first of PENTATRAP's five traps and transported down to their individual traps.

Due to the five stacked Penning traps available, see Fig. 1b, a simultaneous measurement in two traps is possible, increasing the measurement speed by higher statistics and offering up the opportunity for cross checks between the traps
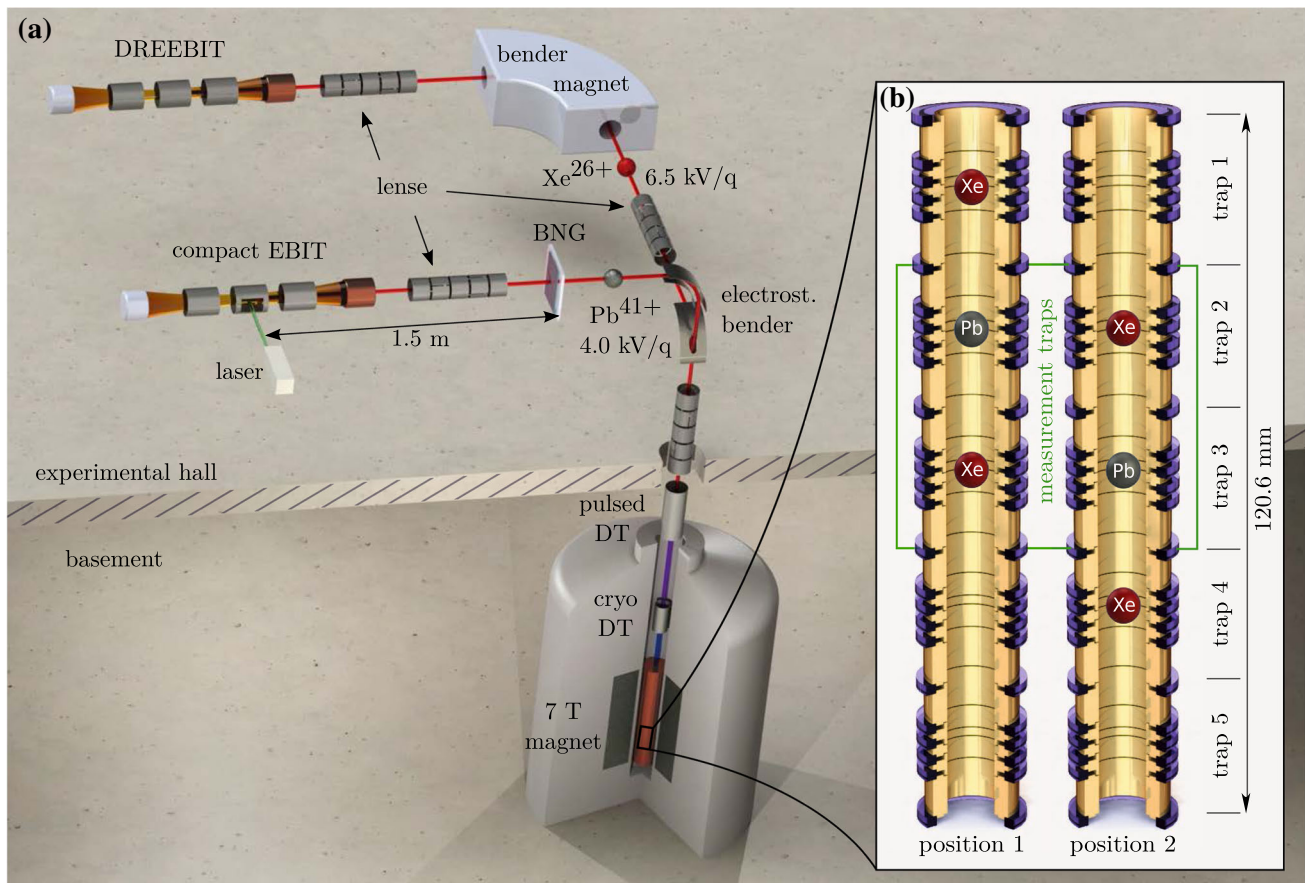
Fig. 1 **a** Schematic illustration of the ion production section, the two beamlines, and the combined deceleration region ending in the trap chamber. The ion bunches with their respective energies are shown after they have been q/m selected by the bender magnet or the Bradbury-Nielson gate (BNG). **b** Schematic drawing of the Penning-trap tower with two measurement ion configurations. The ions are moved from position 1–2 or back every ≈ 15 min. The frequency measurements are carried out in traps 2 and 3. Traps 1 and 4 are utilized as storage traps and trap 5 is currently not in use but is planned to be used to monitor magnetic field fluctuations in the future

and several analysis methods. Out of the other three traps, two are needed for ion storage and one trap is planned for monitoring, however, currently not in use.

The ion's frequencies depend on the magnetic field and the electrostatic potential. All environmental influences on these quantities need to be stabilized over the duration of the measurement. For this, the PENTATRAP laboratory is temperature-stabilized to $\delta T < 50$ mK/h and the height of the liquid helium level z_{lHe} used for cooling the superconducting magnet, Penning traps, and the detection system is stabilized to $\delta z_{lHe} < 1$ mm/h along with the pressure of helium gas inside the magnet's bore to $\delta p < 10$ μbar/h [15].

We employ the Fourier-transform ion-cyclotron-resonance detection technique [25] using cryogenic tank circuits connected to the Penning traps to pick up the small image current induced in the trap electrodes by the ion. The largest frequency ω_+, and therefore the frequency with the highest contribution to the overall error, is measured using the phase-sensitive pulse and phase (PnP) method [26,27]. This

method, described in more detail below, sets an initial phase of the reduced cyclotron frequency, then the motion is left decoupled for a variable phase accumulation time t_{acc} during which the phase can evolve freely, before reading out the final phase ϕ_{meas}. The other two frequencies ω_z and ω_- are measured with the Fast-Fourier-Transform (FFT) dip and the double-dip technique, respectively [28].

The measurements of $^{208}Pb^{41+}$ versus $^{132}Xe^{26+}$ were carried out with the measurement scheme shown in Fig. 2. After a rough estimate of all three frequencies of both ions in both positions, shown in Fig. 1b, using the dip and double-dip technique, the measurement run starts with an N determination, with N being the integer number of full turns of the reduced cyclotron motion during the phase accumulation time. This preparatory measurement is necessary before the actual PnP measurement because the cyclotron phase of the ion increases linearly with time with the increment of the frequency ω_+ and will thereby pass a full turn of 2π many times during the phase accumulation time. The inte-
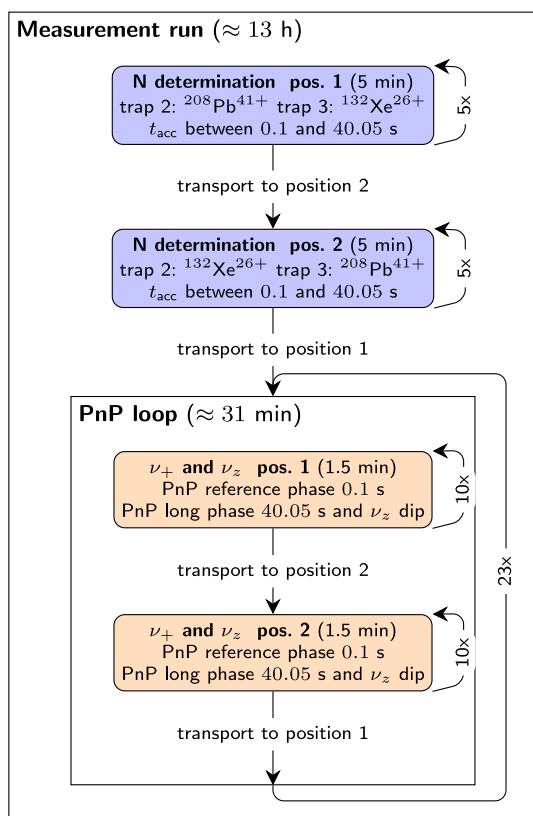
```
┌─────────────────────────────────────────────────┐
│ Measurement run (≈ 13 h)                          │
│   ┌───────────────────────────────────────┐      │
│   │ N determination  pos. 1 (5 min)        │  ⤺   │
│   │ trap 2: ²⁰⁸Pb⁴¹⁺ trap 3: ¹³²Xe²⁶⁺      │  5×  │
│   │ t_acc between 0.1 and 40.05 s          │      │
│   └───────────────────────────────────────┘      │
│                transport to position 2            │
│   ┌───────────────────────────────────────┐      │
│   │ N determination  pos. 2 (5 min)        │  ⤺   │
│   │ trap 2: ¹³²Xe²⁶⁺ trap 3: ²⁰⁸Pb⁴¹⁺      │  5×  │
│   │ t_acc between 0.1 and 40.05 s          │      │
│   └───────────────────────────────────────┘      │
│                transport to position 1            │
│   ┌─────────────────────────────────────────────┐│
│   │ PnP loop (≈ 31 min)                          ││
│   │   ┌───────────────────────────────────┐  ⤺  ││
│   │   │ ν₊ and ν_z  pos. 1 (1.5 min)       │  10×││
│   │   │ PnP reference phase 0.1 s          │     ││  23×
│   │   │ PnP long phase 40.05 s and ν_z dip │     ││
│   │   └───────────────────────────────────┘     ││
│   │           transport to position 2            ││
│   │   ┌───────────────────────────────────┐  ⤺  ││
│   │   │ ν₊ and ν_z  pos. 2 (1.5 min)       │  10×││
│   │   │ PnP reference phase 0.1 s          │     ││
│   │   │ PnP long phase 40.05 s and ν_z dip │     ││
│   │   └───────────────────────────────────┘     ││
│   │           transport to position 1            ││
│   └─────────────────────────────────────────────┘│
└─────────────────────────────────────────────────┘
```

Fig. 2 The figure depicts a flowchart of the measurement scheme and the relevant measurement times during the lead mass campaign. In blue at the top one can see the intial N determination followed by the main measurement PnP loop in orange with the simultaneous measurement of axial frequency and modified cyclotron phase. The ions are frequently swapped in order to minimize the magnetic field drift between position 1 and 2

ger N needs to be known in order to determine the modified cyclotron frequency through the total accumulated phase

$$\phi(t_{\mathrm{acc}}) = t_{\mathrm{acc}} \times \omega_+ = 2\pi \times N + \phi_{\mathrm{meas}} , \qquad (6)$$

with ϕ_{meas} being the measured phase at the end of the accumulation time t_{acc}. The N determination utilizes 9 different phase accumulation times between 0.1 and 40.05 s and finds an ω_+ for which each N for all accumulation times is integer.

A constant phase offset, unavoidable due to the phase readout, is cancelled out by subtracting a short reference phase with an accumulation time of 0.1 s from each long measurement phase. After concluding the N determination in both traps for lead and xenon, the actual PnP loop is started, see Fig. 2 lower half. Here, a starting phase is imprinted on the modified cyclotron motion by an ω_+ dipole excitation pulse. The phase can then evolve freely for t_{acc} before the final modified cyclotron phase is imprinted on the axial motion by a coupling π-pulse, where it can be detected as an axial phase [26,27]. All excitation and coupling pulses are shaped with a Tukey window [29] in order to avoid systematic phase

shifts during the phase readout. During the phase evolution time of the PnP sequence, an FFT axial-dip measurement is performed. This simultaneous phase determination and dip detection leads to a reduction of systematic effects associated with the temporal variation of the trap potential and the magnetic field, since they cancel out when calculating the free cyclotron frequency, using the invariance theorem in Eq. (5). After repeating the measurement of the two ions in trap 2 and 3 ten times, the ions are swapped. If $^{132}\mathrm{Xe}^{26+}$ was in the trap, then $^{208}\mathrm{Pb}^{41+}$ is swapped in and vice versa. This is repeated for around 12 hours before restarting the whole measurement scheme again with the N determination. The magnetron frequency, being a factor $\approx 1,600$ smaller than the modified cyclotron frequency, does not need to be measured repeatedly since the double-dip determination during the preparation phase is sufficiently precise. After one measurement run a relative statistical uncertainty of $\approx 10^{-11}$ is reached.

To determine a neutral mass of $^{208}\mathrm{Pb}$ from the ions' free cyclotron frequency ratio we need to include the mass of the missing electrons in combination with their binding energies (in the following we always refer to the absolute binding energies). We employ the *ab initio* fully relativistic multiconfiguration Dirac–Hartree–Fock (MCDHF) method [30–32] to compute the binding energies E_{Xe} and E_{Pb} of the outermost 26 and 41 electrons, respectively, in neutral Xe and Pb atoms. First, for the case of Xe, the ionization energy of the outermost 8 electrons has been experimentally determined to be of 424.7(7) eV [33]. Thus, one only needs to calculate the binding-energy difference between the ground states of Xe^{26+} ([Ar]$3d^{10}$ $^1S_0$) and Xe^{8+} ([Kr]$4d^{10}$ $^1S_0$). Similarly, since the ionization energy of the outermost 4 electrons in neutral Pb has been measured to be 96.719 04(61) eV [33], only the corresponding binding-energy difference between the ground states of Pb^{41+} ([Kr]$4d^5$ $^4P_{5/2}$) and Pb^{4+} ([Xe]$4f^{14}5d^{10}$ $^1S_0$) needs to be determined theoretically. In the following, we use $E_{\mathrm{Xe}^{08-26}}$ and $E_{\mathrm{Pb}^{04-41}}$ to represent these two terms.

Within the MCDHF scheme, the many-electron atomic state function (ASF) is constructed as a linear combination of configuration state functions (CSFs) with common total angular momentum (J), magnetic (M), and parity (P) quantum numbers: $|\Gamma PJM\rangle = \sum_k c_k |\gamma_k PJM\rangle$. The CSFs $|\gamma_k PJM\rangle$ are given as jj-coupled Slater determinants of one-electron orbitals, and γ_k summarizes all the information needed to fully define the CSF, i.e. the orbital occupation and coupling of single-electron angular momenta. Γ collectively denotes all the γ_k included in the representation of the ASF. The set of CSF basis is generated by the GRASP2018 code [32] via single and double (SD) excitation of electrons from the reference configurations to high-lying virtual orbitals. After solving the self-consistent MCDHF equations for the radial wavefunctions and the mixing coefficients c_k, the rel-

ativistic configuration interaction (RCI) method is applied to account for the corrections arising from the quantum electrodynamic terms and Breit interactions. We systematically expand the size of the basis set by adding and optimizing virtual orbitals layer by layer up to $n = 10$ (n is the principle quantum number), with the final correlation energies being derived by extrapolating to $n = \infty$.

As the ground states of Xe^{26+} and Xe^{8+} are both in closed-shell configurations, the CSF basis sets used for the calculations can be generated by allowing SD excitations from all the core electrons starting with the $1s$ orbitals. This gives a contribution from the SD electron correlation energy of 25.6 eV. The contributions from the Breit interactions and QED effects are 4.0 and 0.5 eV, respectively.

For the calculation of Pb^{41+}, however, due to its open $4d^5$ configuration, the number of CSFs for $J = 5/2$ easily grows above 4 million even for the SD exchanges of the $4s^2 4p^6 4d^5$ electrons and becomes not tractable. Therefore, to access $E_{Pb^{04-41}}$, one needs to construct an ion chain in the calculation to reduce the errors. We first calculate the binding-energy difference between Pb^{4+} and Pb^{22+} via SD excitations from core electrons down to the $3p$ subshell, and then calculate the binding-energy difference between Pb^{22+} and Pb^{36+} by allowing SD excitations of all the core electrons. Finally, the connection between Pb^{36+} and Pb^{41+} is bridged over Pb^{42+} via SD excitations from the $4s$ orbitals. In total, the SD electron correlation effects contribute 58.1 eV to $E_{Pb^{04-41}}$. The Breit interactions and QED terms give rise to corrections of 9.3 and -0.6 eV, respectively, to the binding energy difference.

Until now, only the SD correlation energies are included in the calculations. Considering that the uncertainties in Breit and QED terms are small, the neglected higher-order correlations will account for the systematic errors. To estimate these errors, we make use of the accurate ionization data of the outermost 8 and 4 electrons in Xe and Pb, respectively. The estimations are based on three observations. First, as a self-consistent theory, the MCDHF always approaches the real ground-state energy from above. Thus, the MCDHF binding energy of a given ionic ground state is always smaller than its real value. Second, for a given element, the contributions from higher-order correlation terms scale with the number of bound electrons. Therefore, the differences between the MCDHF binding energy and its real value is more likely to be smaller in highly charged ions. Lastly, within the same isoelectronic sequence, the contributions from higher-order correlations are always smaller for highly charged ions. This is because, perturbatively, in the denominator of each perturbation term, the energy differences between atomic states in highly charged ions are much larger than those in lower charged ions. As a result, for closed-shell ions, the calculated binding-energy differences based on the SD excitations are always smaller than their real values, but their deviations become narrower when the charge states become larger.

For the case of Xe, we find that the calculated binding-energy difference between Xe^{8+} and Xe is 3.5 eV smaller than the experimentally measured value of 424.7(7) eV, with the single-electron ionization energies of Xe, Xe^{7+}, and Xe^{8+} being 0.32 eV, 0.22 eV and 0.10 eV, respectively, smaller than their experimental measurements. Though the deviations of the single-electron ionization energies for some open-shell ions between Xe^{8+} and Xe^{26+} may be larger than the 0.22 eV deviation of that in Xe^{7+}, one can still conservatively expect that the average deviation of the 16 electrons will not be larger than 0.22 eV. This indicates that the systematic shift of $E_{Xe^{08-26}}$ shall be within 4.0 eV. To cover the range between 0 to 4.0 eV, one can add a systematic correction of 2.0(2.0) eV, with both systematic shift and uncertainty being 2.0 eV. This leads to $E_{Xe^{08-26}} = 8546.5(2.0)$ eV and $E_{Xe} = 8971.2(2.1)$ eV.

With a similar procedure, the ionization energy of Pb^{2+} and Pb^{3+} are found to be 1.26 and 0.95 eV smaller than their experimental measured values when SD excitation from the $3p$ subshells are considered. This indicates an average deviation of < 1.0 eV for the single-electron ionization energies for Pb^{4+} to Pb^{22+}, and a systematic correction of 9.0(9.0) eV to the binding energy of the corresponding 18 electrons. For the ions between Pb^{22+} and Pb^{41+}, since they are close to the isoelectronic systems of Xe ions, one can conservatively assume a < 0.22 eV average deviation of the corresponding single-electron ionization energies. After the summation, we obtain $E_{Pb^{04-41}} = 28633.9(9.1)$ eV and $E_{Pb} = 28730.6(9.1)$ eV.

3 Results

After calculating the free cyclotron frequencies during each PnP loop, the interpolation method [34] is applied to calculate the frequency ratios, see Fig. 3. This method uses two consecutive cyclotron frequencies of one trap in position 1 and interpolates them to the time the cyclotron frequency of the position 2 in the same trap was measured. Then the frequency ratio of the interpolated value of position 1 and the matching value of position 2 can be formed cancelling out in first order the magnetic field drift over time. The linear drift of the magnetic field is $\Delta B/B = -2.3 \times 10^{-10}$ /h. The impact of the non-linear drifts of the B-field was thoroughly investigated and found insignificant on the level of the achieved statistical uncertainty. The final measured ion frequency ratio is
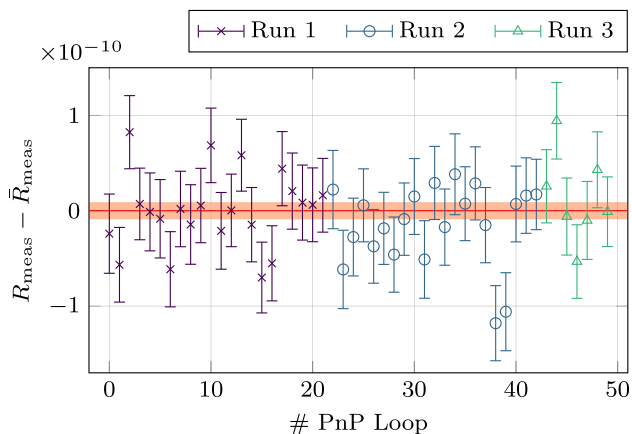
Fig. 3 The plot shows the frequency ratios for the different PnP loops. Each color represents a different measurement run. The 1σ error band of the averaged ratio $\bar{R}_{\text{meas}}$ is visualized in red

Table 1 Systematic shifts and their uncertainties on the measured modified-cyclotron frequency ratio R_{meas}. For more details see text

Effect	Correction to R_{meas} (10^{-12})	Uncertainty (10^{-12})
Image charge shift	185	9
Relativistic shift	0	4
Total	185	10

$$R_{\text{meas}} - 1 = \frac{\nu(^{208}\text{Pb}^{41+})}{\nu(^{132}\text{Xe}^{26+})} - 1$$
$$= 1.252\,194\,24(9) \times 10^{-4}, \tag{7}$$

with a relative statistical uncertainty of 9×10^{-12}.

The measured ratio is then corrected for known systematic shifts and their respective uncertainties. An overview of the relevant systematic effects and their size is listed in Table 1.

The largest systematic shift comes from the image charge shift (ICS) [35]. The highly charged ions induce an oscillating image charge in the trap electrodes. While this is necessary for detection, it causes a shift of the ions' frequencies by generating a counteracting electric field. The image charge shift depends strongly on the mass difference of the ions and on the radius of the trap, the latter being in the case of PENTATRAP 5.000(5) mm. The ICS was determined to be $R_{\text{meas}} - \tilde{R} = \Delta(R_{\text{meas}})_{\text{ICS}} = 1.85(9) \times 10^{-10}$, with $\tilde{R}$ being the corrected ratio. In addition to this, the relativistic shift due to relativistic mass increase [36] leads to another systematic uncertainty related to the size of the excited radii during the PnP measurement scheme: $\Delta(R_{\text{meas}})_{\text{rel}} = 0(4) \times 10^{-12}$.

All other known systematic effects, due to e.g. trap potential anharmonicity, are on the order of 10^{-13} and below and are therefore neglected. Thus, the final ω_c-ratio is $R - 1 =$
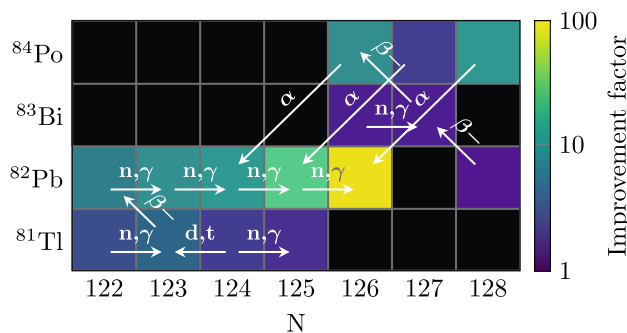
Fig. 4 This colormap depicts a cutout of the nuclide chart. The color corresponds to the improvement factor (with 1 being no improvement) in mass precision after including the new mass value of ^{208}Pb in the AME [6]. The labeled arrows show the relevant connections for the mass determination of the different nuclides via different forms of decays from which the energy is known

$1.252\,192\,39(9)(10)(13) \times 10^{-4}$, where the number in the first, second, and third brackets indicate the statistical, systematic, and total uncertainty, respectively.

Combining the binding energies of the missing electrons calculated by theory, the experimentally determined mass ratio, and the mass excess of the reference isotope of ^{132}Xe [13,14] as listed in the AME2020, the mass excess of ^{208}Pb is determined to be $-21749.855(13)$ keV, which amounts to a neutral atomic mass of $207.976\,650\,571(14)$ u. The new value improves the mass uncertainty of neutral ^{208}Pb by a factor of 88 to a relative uncertainty of $\delta m/m = 7 \times 10^{-11}$ and shifts the mass excess value by $-1.4(1.1)$ keV.

4 Discussion and conclusion

In addition to the improvement of precision of the mass of ^{208}Pb itself, our measurement also improves the masses of a series of lead isotopes, connected by (n, γ) reactions. So far, their mass precision was limited by the precision of ^{208}Pb, but is now limited by the precision of the energy of the (n, γ) reactions. Furthermore, Fig. 4 shows the improvement in precision of, in total, 14 neighbouring nuclides' masses connected to the mass of ^{208}Pb via different decays, e.g. α decay, for which the energy is well known. Since the new value of the mass excess of ^{208}Pb is shifted downward, all these connected nuclides will be shifted down by 1.4 keV. Table 2 lists the new mass values for all nuclides which were significantly improved. With the reported measurement we have established a new region in the nuclear chart with reference masses for experiments on heavy and superheavy nuclides. When measuring masses around $m = 200$ u the error due to the reference mass will be as low as a few 10^{-10} and therefore negligible for mass determinations on radionuclides.

Furthermore, with the new mass precision of ^{208}Pb of 7×10^{-11} the g-factor of the bound electron can be determined

Table 2 New mass values of affected nuclides, when including the new mass value of ^{208}Pb in the AME2020 [6]

Z	A	el.	$T_{1/2}$ [37]	AME2020 mass (μu)		Improved mass (μu)		Improvement factor
81	203	Tl	Stable	202,972,344.1	(1.3)	202,972,342.7	(0.4)	3.2
81	204	Tl	3.783(12) y	203,973,863.4	(1.2)	203,973,862.01	(0.26)	4.8
82	204	Pb	$1.4(6) \times 10^{17}$ y	203,973,043.5	(1.2)	203,973,042.09	(0.18)	7.0
81	205	Tl	Stable	204,974,427.3	(1.3)	204,974,425.9	(0.6)	2.4
82	205	Pb	$1.70(9) \times 10^{7}$ y	204,974,481.7	(1.2)	204,974,480.26	(0.13)	9.2
81	206	Tl	4.202(11) min	205,976,110.1	(1.4)	205,976,108.7	(0.7)	2.1
82	206	Pb	Stable	205,974,465.2	(1.2)	205,974,463.79	(0.12)	10.6
82	207	Pb	Stable	206,975,896.8	(1.2)	206,975,895.39	(0.06)	21.6
82	208	Pb	Stable	207,976,652.0	(1.2)	207,976,650.571	(0.014)	88.0
83	209	Bi	$2.01(8) \times 10^{19}$ y	208,980,398.6	(1.5)	208,980,397.2	(0.8)	1.8
82	210	Pb	22.20(22) y	209,984,188.4	(1.6)	209,984,187	(1.0)	1.6
83	210	Bi	5.012(5) d	209,984,120.2	(1.5)	209,984,118.9	(0.8)	1.8
84	210	Po	138.376(2) d	209,982,873.7	(1.2)	209,982,872.27	(0.14)	8.8
84	211	Po	0.516(3) s	210,986,653.2	(1.3)	210,986,651.7	(0.6)	2.4
84	212	Po	294.3(8) ns	211,988,868.0	(1.2)	211,988,866.55	(0.12)	10.1

to the same level of precision. It therefore allows to carry out the experiments on ^{208}Pb^{81+} at Alphatrap and Artemis without having a large mass dependent error limiting their g-factor determination.

References

1. Y.T. Oganessian, V.K. Utyonkov, Y.V. Lobanov, F.S. Abdullin, A.N. Polyakov, R.N. Sagaidak, I.V. Shirokovsky, Y.S. Tsyganov, A.A. Voinov, G.G. Gulbekian, S.L. Bogomolov, B.N. Gikal, A.N. Mezentsev, S. Iliev, V.G. Subbotin, A.M. Sukhov, K. Subotic, V.I. Zagrebaev, G.K. Vostokin, M.G. Itkis, K.J. Moody, J.B. Patin, D.A. Shaughnessy, M.A. Stoyer, N.J. Stoyer, P.A. Wilk, J.M. Kenneally, J.H. Landrum, J.F. Wild, R.W. Lougheed, Phys. Rev. C **74**(4), 044602 (2006). https://doi.org/10.1103/PhysRevC.74.044602
2. M. Block, D. Ackermann, K. Blaum, C. Droese, M. Dworschak, S. Eliseev, T. Fleckenstein, E. Haettner, F. Herfurth, F.P. Heßberger, S. Hofmann, J. Ketelaer, J. Ketter, H.J. Kluge, G. Marx, M. Mazzocco, Y.N. Novikov, W.R. Plaß, A. Popeko, S. Rahaman, D. Rodríguez, C. Scheidenberger, L. Schweikhard, P.G. Thirolf, G.K. Vorobyev, C. Weber, Nature **463**(7282), 785 (2010). https://doi.org/10.1038/nature08774
3. M. Dworschak, M. Block, D. Ackermann, G. Audi, K. Blaum, C. Droese, S. Eliseev, T. Fleckenstein, E. Haettner, F. Herfurth, F.P. Heßberger, S. Hofmann, J. Ketelaer, J. Ketter, H.J. Kluge, G. Marx, M. Mazzocco, Y.N. Novikov, W.R. Plaß, A. Popeko, S. Rahaman, D. Rodríguez, C. Scheidenberger, L. Schweikhard, P.G. Thirolf, G.K. Vorobyev, M. Wang, C. Weber, Phys. Rev. C **81**(6), 064312 (2010). https://doi.org/10.1103/PhysRevC.81.064312
4. E.M. Ramirez, D. Ackermann, K. Blaum, M. Block, C. Droese, C.E. Düllmann, M. Dworschak, M. Eibach, S. Eliseev, E. Haettner, F. Herfurth, F.P. Heßberger, S. Hofmann, J. Ketelaer, G. Marx, M. Mazzocco, D. Nesterenko, Y.N. Novikov, W.R. Plaß, D. Rodríguez, C. Scheidenberger, L. Schweikhard, P.G. Thirolf, C. Weber, Science **337**(6099), 1207 (2012). https://doi.org/10.1126/science.1225636
5. M. Eibach, T. Beyer, K. Blaum, M. Block, C.E. Düllmann, K. Eberhardt, J. Grund, S. Nagy, H. Nitsche, W. Nörtershäuser, D. Renisch, K.P. Rykaczewski, F. Schneider, C. Smorra, J. Vieten, M. Wang, K. Wendt, Phys. Rev. C **89**(6), 064318 (2014). https://doi.org/10.1103/PhysRevC.89.064318
6. M. Wang, W.J. Huang, F.G. Kondev, G. Audi, S. Naimi, Chin. Phys. C **45**(3), 030003 (2021). https://doi.org/10.1088/1674-1137/abddaf

7. A. Kellerbauer, K. Blaum, G. Bollen, F. Herfurth, H.J. Kluge, M. Kuckein, E. Sauvan, C. Scheidenberger, L. Schweikhard, Eur. Phys. J. D **22**(1), 53 (2003). https://doi.org/10.1140/epjd/e2002-00222-0

8. J. Ketelaer, J. Krämer, D. Beck, K. Blaum, M. Block, K. Eberhardt, G. Eitel, R. Ferrer, C. Geppert, S. George, F. Herfurth, J. Ketter, S. Nagy, D. Neidherr, R. Neugart, W. Nörtershäuser, J. Repp, C. Smorra, N. Trautmann, C. Weber, Nuclear instruments and methods in physics research section a: accelerators. Spectromet. Detect. Assoc. Equip. **594**(2), 162 (2008). https://doi.org/10.1016/j.nima.2008.06.023

9. J. Grund, M. Asai, K. Blaum, M. Block, S. Chenmarev, C.E. Düllmann, K. Eberhardt, S. Lohse, Y. Nagame, S. Nagy, P. Naubereit, J.J.W. van de Laar, F. Schneider, T.K. Sato, N. Sato, D. Simonovski, K. Tsukada, K. Wendt, Nuclear instruments and methods in physics research section a: accelerators. Spectromet. Detect. Assoc. Equip. **972**, 164013 (2020). https://doi.org/10.1016/j.nima.2020.164013

10. S. Sturm, F. Köhler, J. Zatorski, A. Wagner, Z. Harman, G. Werth, W. Quint, C.H. Keitel, K. Blaum, Nature **506**(7489), 467 (2014). https://doi.org/10.1038/nature13026

11. M. Vogel, M.S. Ebrahimi, Z. Guo, A. Khodaparast, G. Birkl, W. Quint, Annalen der Physik **531**(5), 1800211 (2019). https://doi.org/10.1002/andp.201800211

12. F. Köhler, K. Blaum, M. Block, S. Chenmarev, S. Eliseev, D.A. Glazov, M. Goncharov, J. Hou, A. Kracke, D.A. Nesterenko, Y.N. Novikov, W. Quint, E. Minaya Ramirez, V.M. Shabaev, S. Sturm, A.V. Volotka, G. Werth, Nat. Commun. **7**(1), 10246 (2016). https://doi.org/10.1038/ncomms10246

13. M. Redshaw, B.J. Mount, E.G. Myers, Phys. Rev. A **79**(1), 012506 (2009)

14. A. Rischka, H. Cakir, M. Door, P. Filianin, Z. Harman, W.J. Huang, P. Indelicato, C.H. Keitel, C.M. König, K. Kromer, M. Müller, Y.N. Novikov, R.X. Schüssler, C. Schweiger, S. Eliseev, K. Blaum, Phys. Rev. Lett. **124**(11), 113001 (2020). https://doi.org/10.1103/PhysRevLett.124.113001

15. J. Repp, C. Böhm, J.R. Crespo López-Urrutia, A. Dörr, S. Eliseev, S. George, M. Goncharov, Y.N. Novikov, C. Roux, S. Sturm, S. Ulmer, K. Blaum, Appl. Phys. B **107**(4), 983 (2012). https://doi.org/10.1007/s00340-011-4823-6

16. C. Roux, C. Böhm, A. Dörr, S. Eliseev, S. George, M. Goncharov, Y.N. Novikov, J. Repp, S. Sturm, S. Ulmer, K. Blaum, Appl. Phys. B **107**(4), 997 (2012). https://doi.org/10.1007/s00340-011-4825-4

17. J. Zatorski, B. Sikora, S.G. Karshenboim, S. Sturm, F. Köhler-Langes, K. Blaum, C.H. Keitel, Z. Harman, Phys. Rev. A **96**(1), 012502 (2017). https://doi.org/10.1103/PhysRevA.96.012502

18. L.S. Brown, G. Gabrielse, Phys. Rev. A **25**(4), 2423 (1982). https://doi.org/10.1103/PhysRevA.25.2423

19. V.P. Ovsyannikov, G. Zschornack, Rev. Sci. Instrum. **70**(6), 2646 (1999). https://doi.org/10.1063/1.1149822

20. Startseite » DREEBIT GmbH - DREEBIT Company | DE. https://www.dreebit.com/de/

21. P. Micke, S. Kühn, L. Buchauer, J.R. Harries, T.M. Bücking, K. Blaum, A. Cieluch, A. Egl, D. Hollain, S. Kraemer, T. Pfeifer, P.O. Schmidt, R.X. Schüssler, C. Schweiger, T. Stöhlker, S. Sturm, R.N. Wolf, S. Bernitt, J.R. Crespo López-Urrutia, Rev. Sci. Instrum. **89**(6), 063109 (2018). https://doi.org/10.1063/1.5026961

22. C. Schweiger, C.M. König, J.R. Crespo López-Urrutia, M. Door, H. Dorrer, C.E. Düllmann, S. Eliseev, P. Filianin, W. Huang, K. Kromer, P. Micke, M. Müller, D. Renisch, A. Rischka, R.X. Schüssler, K. Blaum, Rev. Sci. Instrum. **90**(12), 123201 (2019). https://doi.org/10.1063/1.5128331

23. C. Schweiger, et al., in preparation (2021)

24. N.E. Bradbury, R.A. Nielsen, Phys. Rev. **49**(5), 388 (1936). https://doi.org/10.1103/PhysRev.49.388

25. A.G. Marshall, C.L. Hendrickson, G.S. Jackson, Mass Spectrom. Rev. **17**(1), 1 (1998). https://doi.org/10.1002/(SICI)1098-2787(1998)17:1<1::AID-MAS1>3.0.CO;2-K

26. E.A. Cornell, R.M. Weisskoff, K.R. Boyce, R.W. Flanagan, G.P. Lafyatis, D.E. Pritchard, Phys. Rev. Lett. **63**(16), 1674 (1989). https://doi.org/10.1103/PhysRevLett.63.1674

27. E.A. Cornell, R.M. Weisskoff, K.R. Boyce, D.E. Pritchard, Phys. Rev. A **41**(1), 312 (1990). https://doi.org/10.1103/PhysRevA.41.312

28. X. Feng, M. Charlton, M. Holzscheiter, R.A. Lewis, Y. Yamazaki, J. Appl. Phys. **79**(1), 8 (1996). https://doi.org/10.1063/1.360947

29. F. Harris, Proc. IEEE **66**(1), 51 (1978). https://doi.org/10.1109/PROC.1978.10837

30. I.P. Grant, Adv. Phys. **19**, 747 (1970)

31. J.P. Desclaux, D.F. Mayers, F. O'Brien, J. Phys. B **4**, 631 (1971)

32. C.F. Fischer, G. Gaigalas, P. Jönsson, J. Bieroń, Comput. Phys. Commun. **237**, 184 (2019)

33. A. Kramida, Yu. Ralchenko, J. Reader, and NIST ASD Team. NIST Atomic Spectra Database (ver. 5.8), [Online]. Available: https://physics.nist.gov/asd [2021, August 11]. National Institute of Standards and Technology, Gaithersburg, MD (2020)

34. M. Door, et al., in preparation (2021)

35. M. Schuh, F. Heiße, T. Eronen, J. Ketter, F. Köhler-Langes, S. Rau, T. Segal, W. Quint, S. Sturm, K. Blaum, Phys. Rev. A **100**(2), 023411 (2019). https://doi.org/10.1103/PhysRevA.100.023411

36. L.S. Brown, G. Gabrielse, Rev. Mod. Phys. **58**(1), 233 (1986). https://doi.org/10.1103/RevModPhys.58.233

37. IAEA Nuclear Data Services. https://www-nds.iaea.org/